

Chapter 5: BOOMERANG at the Micron Scale and Below

5.0 Introduction

The availability of a general NMR method whose sensitivity persists down to size scales that are fundamentally inaccessible to inductive detection motivates speculation regarding applications. The observation of NMR from nanoliter samples with inductive detection in microcoils with moderately concentrated samples^{1,2} is near the lower size limit where inductive detection is predicted to be competitive with BOOMERANG for proton-bearing samples at conveniently available static field strengths. As we noted in Chapter 2, this crossover limit is at larger size scales for almost all other nuclei and for the lower (~ 2 T) field strengths that are practical with static fields generated by ferromagnets. Thus, BOOMERANG is being developed^{3,4} as the NMR method of choice for low-power, low-cost, portable devices for NMR in remote environments such as in space exploration. Portable NMR here on Earth is also of interest for convenience or for high-throughput tasks, and so inexpensive 2 T spectrometer units for laboratory glove boxes or dip-probes for use in industrial process streams are candidate applications for commercialization of BOOMERANG technology.

Just as interesting is NMR at the higher fields available in commercial superconducting magnets. There are many samples in the ~ 0.1 - $100 \mu\text{m}$ size range that, according to estimates in Chapter 2, would exhibit satisfactory signal-to-noise with acceptable signal averaging. The main motivation here is in cases where sample size is limited intrinsically, such as in forensics, or when it is desirable to examine systems one at a time rather than in ensemble average. For example, BOOMERANG might allow spectroscopy and imaging of individual cells or membranes *in situ* or rotation studies on individual protein or zeolite crystallites that may be too small for use in crystallography. Another area of application at somewhat smaller scales is quantum dots.

The ability to measure NMR on a sample containing $10^9 - 10^{12}$ spins would also enable NMR spectra of molecular monolayers and other surface species. There are special geometric considerations to be taken into account in surface studies and some of these are treated in section 5.3. An ultimate goal in designs for BOOMERANG at the micron scale is a microfabricated array of BOOMERANG spectrometers, which would allow massively parallel NMR analysis of sample libraries used in combinatorial-chemistry approaches to all kinds of problems in materials science, catalysis, and biochemistry.

Clearly there is sufficient motivation for NMR devices at length scales where the sensitivity of BOOMERANG is adequate but that of inductive methods is not. We have predicted on grounds of sensitivity and resolution that BOOMERANG methods show great promise as the means of extending NMR into the realm of smaller samples in a general way. However, in our analysis of sensitivity in both

force and induction methods, we have considered only instrument noise due to thermal processes in the detector. We now consider a new noise source that comes from the sample itself: spin noise.

Spin noise is uncertainty in the measured values of spectral parameters due to fluctuations in the sample's initial magnetization. It is present, independent of detection method, whenever measurements must be repeated on a standard initial state, such as in signal averaging or in the time-sequencing methods described in Chapter 4. In the context of proposals for very high sensitivity MRFM of biomolecules⁵, (where, for more than one target spin, it may turn out to be a show-stopper), it has been largely ignored.

5.1 Spin Noise

The problem is best illustrated by example. Suppose we have a 0.8 ml room-temperature liquid sample 0.002 M in an organic compound and we wish to measure its single-quantum ¹³C NMR spectrum at 125 MHz. If we have a single carbon site of interest per molecule, this sample contains 10¹⁸ of the target spins. The sample's magnetization can be calculated with the Curie law, which may be written

$$M = \frac{\bar{N}\hbar\gamma}{2} \frac{\hbar\gamma B}{2k_B T} \quad (5.1)$$

at high temperature T for spin- $\frac{1}{2}$ nuclei with magnetogyric ratio γ at spin density \bar{N} in a static field B . This formula contains the polarization,

$$\rho = \tanh\left(\frac{\hbar\gamma B}{2k_B T}\right) \approx \frac{\hbar\gamma B}{2k_B T}, \quad (5.2)$$

which is 10^{-5} for the present case. Since the sample contains 10^{18} spins, and the equilibrium polarization is 10^{-5} , the net magnetization available to drive the detection apparatus is that of only 10^{13} spins.

The total magnetization is the sum of the magnetic moments of N spins per unit volume, each of which has a roughly but not exactly equal probability of contributing $+1$ or -1 nuclear moments to the magnetization when the polarization is much less than unity (we shall make this more precise later, but for now, the error statistics are nearly those of flipping a very slightly weighted coin). The uncertainty in the initial magnetization is proportional to \sqrt{N} . For the 10^{18} spin sample, this fluctuation magnetization, which manifests as shot-to-shot variations in the initial magnetization, is that of 10^9 spins, only 0.01% of the signal. The distribution of values of initial magnetization is shown schematically in Figure 5.1 a.

The situation is entirely different for the case of 10^5 spins (*e.g.*, a moderately concentrated species coating a single $1 \mu\text{m}$ diameter cell). Here, the average signal magnetization at room temperature in a 125 MHz field corresponds to that of only one spin on average, while the shot-to-shot fluctuations in magnetization are proportional to $\sqrt{N} \approx 300$ spins. The distribution for this case is shown in Figure 5.1 b. In a time-sequenced experiment, these fluctuations in initial magnetization manifest as so-called t_1 noise, which in this case is 300 times larger than the signal per root shot, even in the case of no instrument noise.

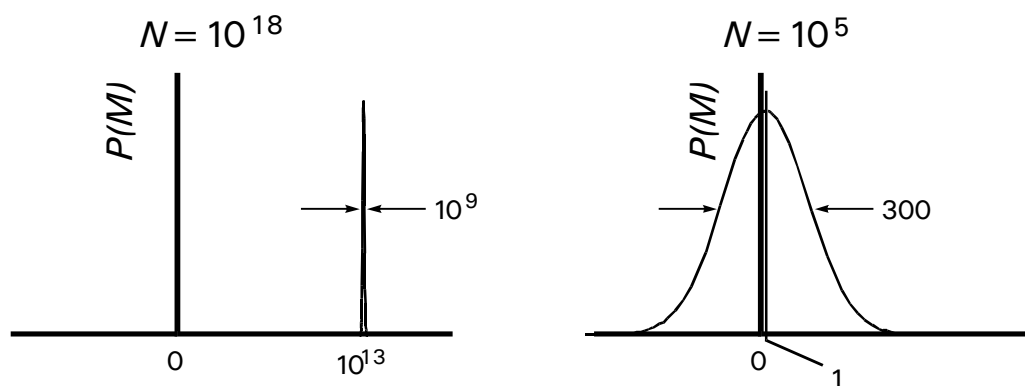


Figure 5.1. (a) Probability distribution for the net magnetization of $N = 10^{18}$ spins at thermal equilibrium with polarization 10^{-5} . The distribution is very sharply peaked, as the polarization ρ is significantly larger than $N^{-1/2}$. (b) Probability distribution for the net magnetization of $N = 10^5$ spins. Here the variance of the (roughly binomial) distribution is substantially larger than the mean. Note also that values of opposite sign from the mean are about as probable as values having the same sign.

The solution to the problem is in recognizing that in general we are interested in parameters in a spin Hamiltonian and not particularly in the magnetization *per se*. In fact, a look at the vast majority of published NMR spectra shows no units on the “y-axis” (or other ordinate axis if we are looking at multidimensional spectra). What we care about is a *correlation function* or its spectrum: the Bohr frequencies, relaxation times, coupling constants, and *relative* amplitudes in spectroscopy, or some kind of contrast observable in imaging.

5.2 Correlated Observations Narrow Quantum Uncertainty, Enhancing Spectroscopic Transients (CONQUEST)

Figure 5.2 shows the time sequence used in Chapter 4 to encode the single-quantum FT-NMR spectrum, here modified to include a second detection period (an

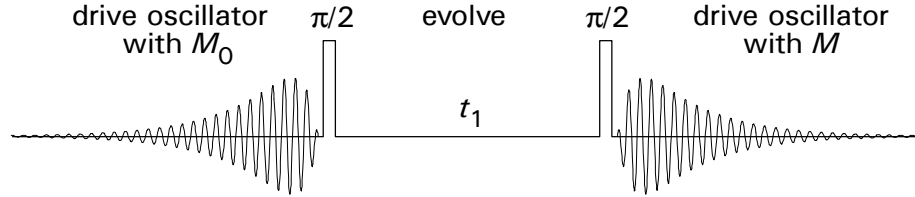


Figure 5.2. Time sequence for the CONQUEST method of encoding spectra pointwise. As in the first-order method (figure 4.3), two $\pi/2$ pulses are separated by a period t_1 , which is incremented on successive shots of the experiment. The magnetization that survives the evolution period is measured by cyclically inverting it to drive the oscillator. In CONQUEST, a second period of driving is included before the first pulse to measure the fluctuation magnetization at the start of the encoding period. The signal for a given value of t_1 is defined as the product $M_0 M(t_1)$.

oscillator-driving interval) that precedes the evolution period. Consider the time-domain “second-order” signal

$$S_2(t_1) = M_{z,0} M_z(t_1), \quad (5.3)$$

which is formed on a given iteration by multiplying the result of the first measurement by the result of the second. What are the statistics of this signal compared to those of the ordinary (first-order) pointwise signal

$$S_1(t_1) = M_z(t_1)? \quad (5.4)$$

5.2.1 Mean and variance of the signals

We shall consider the simplest case of a sample containing N isochronous spins $\frac{1}{2}$ in a device with negligible instrument noise so that we may reveal the essential features of the spin noise and the method. We shall also drop the units from Equations (5.3) and (5.4), calculating instead with the dimensionless angular momentum expressions

$$S_1(t_1) = I_z(t_1) \quad \text{and} \quad S_2(t_1) = I_{z,0} I_z(t_1). \quad (5.5a,b)$$

With measurements of longitudinal magnetization that are perfectly devoid of instrument noise, the results are always eigenvalues of the operator I_z . The probability of measuring the value m on the first measurement is

$$W(m) = Tr\{P_m \rho_0 P_m\} = Tr\{P_m \rho_0\}. \quad (5.6)$$

Here, ρ_0 is the thermal-equilibrium density operator and P_m is a projection operator associated with the eigenspace belonging to the eigenvalue m . Similarly, the joint probability of measuring the value m on the first measurement and k on the second measurement is

$$W(m, k) = Tr\{P_k U P_m \rho_0 P_m U^\dagger P_k\} = Tr\{U^\dagger P_k U P_m \rho_0\}, \quad (5.7)$$

where U is a time-evolution operator associated with the interval between the two measurements. The equilibrium density operator for this problem is

$$\rho_0 = \frac{1}{Q} e^{-H/k_B T}, \quad (5.8)$$

where

$$H = -\hbar\omega_0 I_z \quad \text{and} \quad Q \equiv Tr\{e^{-H/k_B T}\} \quad (5.9)$$

denote the Hamiltonian and the partition function.

In writing the last equalities in Equations (5.6) and (5.7), we have made use of the invariance of the trace to cyclic permutation of operators in a product, the idempotent property of projection operators ($P_m^2 = P_m$), and the fact that the

equilibrium density operator commutes with projections onto eigenspaces belonging to eigenvalues of the Hamiltonian, which is proportional to I_z .

Equation (5.7) may be used to calculate expectation values and variances for the first- and second-order signals $S_1(t_1)$ and $S_2(t_1)$. For example, the expectation value of $S_2(t_1)$ is found by multiplying the probability distribution $W(m, k)$ by m and k and then summing over all values of m and k :

$$\langle S_2(t_1) \rangle = \sum_{m,k} mkW(m, k) = \sum_{m,k} Tr\{U^\dagger kP_k UmP_m\rho_0\}. \quad (5.10)$$

We then recognize that $mP_m = I_z P_m$ and $\sum_m P_m = \mathbf{1}$ (and similarly for k) and write

$$\langle S_2(t_1) \rangle = Tr\{U^\dagger I_z U I_z \rho_0\} = Tr\{I_z(t_1) I_z \rho_0\} = \langle I_z(t_1) I_z \rangle, \quad (5.11)$$

where

$$I_z(t_1) = U^\dagger I_z U = I_z \cos(\omega t_1) - I_x \sin(\omega t_1) \quad (5.12)$$

is the Heisenberg-representation operator associated with the second measurement of I_z and ω is the Larmor frequency. We proceed similarly for the expectation value of the first-order signal $S_1(t_1)$ and for the variances $\sigma_1^2(t_1) \equiv \langle S_1^2 \rangle - \langle S_1 \rangle^2$ and $\sigma_2^2(t_1) \equiv \langle S_2^2 \rangle - \langle S_2 \rangle^2$ and find

$$\langle S_1(t_1) \rangle = \langle I_z \rangle \cos \omega t_1, \quad (5.13)$$

$$\langle S_2(t_1) \rangle = \langle I_z^2 \rangle \cos \omega t_1, \quad (5.14)$$

$$\sigma_1^2(t_1) = (\langle I_z^2 \rangle - \langle I_z \rangle^2) \cos^2 \omega t_1 + \langle I_x^2 \rangle \sin^2 \omega t_1, \quad (5.15)$$

$$\text{and } \sigma_2^2(t_1) = \left(\langle I_z^4 \rangle - \langle I_z^2 \rangle^2 \right) \cos^2 \omega t_1 + \langle I_x^2 I_z^2 \rangle \sin^2 \omega t_1 \quad (5.16)$$

with the help of Equation (5.12). The expectation values on the right-hand sides of Equations (5.13–16) are with respect to the initial, thermal state ρ_0 . Terms proportional to $\langle I_x \rangle$, $\langle I_x I_z + I_z I_x \rangle$, and $\langle (I_x I_z + I_z I_x) I_z^2 \rangle$ in Equations (5.13–16) are left out because they are easily shown to vanish.

Expectation values of powers of I_z are calculated straightforwardly from a moment generating function,

$$G(s) = \langle e^{isI_z} \rangle. \quad (5.17)$$

Differentiation of $G(s)$ with respect to the argument s yields the expectation values:

$$\langle I_z^n \rangle = (-i)^n \left. \frac{d^n G}{ds^n} \right|_{s=0}. \quad (5.18)$$

$G(s)$ is evaluated in terms of the number of spins N and the polarization p in Appendix D. The result is

$$G(s) = \left(\cos \frac{s}{2} + ip \sin \frac{s}{2} \right)^N. \quad (5.19)$$

In accordance with Equation (5.18), the expectation values of the necessary powers of I_z are listed in Table 5.1. Also necessary are the expectation values $\langle I_x^2 \rangle$ and $\langle I_x^2 I_z^2 \rangle$,

m	$\langle I_z^m \rangle$
1	$\frac{1}{2} Np$
2	$\frac{1}{4} N(1 + (N-1)p^2)$
4	$\frac{1}{16} N \left((3N-2) + 2(3N-4)(N-1)p^2 + (N-3)(N-2)(N-1)p^4 \right)$

Table 5.1. Expectation values of powers of I_z .

which can be calculated from $G'(s) \equiv \langle I_x^2 e^{isI_z} \rangle$. We recognize that in the expansion of the operator $I_x^2 = \left(\sum_i I_{x,i} \right)^2$, cross-terms like $I_{x,j} I_{x,k \neq j} e^{isI_z}$ are traceless, and so we find that $G'(s) = \frac{1}{4} N G(s)$ and that

$$\langle I_x^2 \rangle = \frac{1}{4} N \quad \text{and} \quad \langle I_x^2 I_z^2 \rangle = \frac{1}{4} N \langle I_z^2 \rangle. \quad (5.20a,b)$$

Results from Equations (5.13–20) are combined to compute the expectation values and variances of the first- and second-order signals, which are shown in Table 5.2.

a)	Expectation value	Variance
$S_1(t_1)$	$\frac{1}{2} N p \cos \omega t_1$	$\frac{1}{4} N (1 - p^2 \cos^2 \omega t_1)$
$S_2(t_1)$	$\frac{1}{4} N (1 + (N-1)p^2) \cos \omega t_1$	$\frac{1}{16} N \left(\begin{array}{c} N + (N-2) \cos^2 \omega t_1 \\ + (N + (3N-8) \cos^2 \omega t_1) (N-1) p^2 \\ - (4N-6)(N-1) p^4 \cos^2 \omega t_1 \end{array} \right)$

b)	Expectation value	Variance
$S_1(t_1)$	$\frac{1}{2} N p \cos \omega t_1$	$\frac{1}{4} N$
$S_2(t_1)$	$\frac{1}{4} N \cos \omega t_1$	$\frac{1}{16} N (N + (N-2) \cos^2 \omega t_1)$

Table 5.2. Expectation values and variances of the first- and second-order signals. a) Exact expressions. b) Expressions to leading order in the polarization when $\rho\sqrt{N} \ll 1$.

5.2.2 Remarks

The signal-to-spin-noise ratio SNR_{spin} may be defined as the ratio of the expectation value to the square root of the variance. This quantity falls below unity for the $\cos \omega t_1 = 1$ values of the first-order signal when $\rho\sqrt{N} < 1$. Both the signal

and SNR_{spin} are proportional to the polarization, and in the limit of zero polarization there is no first-order signal that can be built up pointwise.

The signal-to-spin-noise ratio for the second-order signal is entirely different. In the limit of vanishing polarization, SNR_{spin} is independent of the polarization, and it is approximately unity for $N > 1$. A look at expectation values shows that the second-order signal has the same Fourier spectrum as the first-order signal. However, individual shots of the experiment for a given t_1 value can be co-added in the second-order signal without the individual contributors cancelling out on average as they do in the first-order signal when $\rho = 0$. The second order method can be used to measure a spectrum even with no spin order.

It is interesting to note that one can look at the “before” and “after” time series $M_{z,0}(t_1)$ and $M_z(t_1)$ individually, but, in the limit $\rho = 0$, they separately contain no information whatsoever about the spin system. The information in the spectrum is entirely contained in correlations. Under the influence of the pulse sequence and detection protocol, the spin populations determining measurements of I_z exhibit second-order coherence.

The “ring-down” aspect of the oscillator’s motion depicted in Figure 5.2 during both the “before” and “after” detection periods may be somewhat misleading. In Figure 4.3, when a large mean magnetization is used to drive the oscillator on each shot, relaxation processes during the driving interval make the magnetization relax to near zero on average, and this causes a decrease in the oscillator amplitude with time t_2 during detection as shown. When the mean

magnetization is essentially zero to begin with compared to fluctuations, the magnetization used to drive the oscillator can be very far from a value that is indicative of the mean, and in fact it can have the opposite sign. Also, the detector oscillator will have some nonzero thermal amplitude and random phase at the start of a given driving interval, and memory of this information decays in the oscillator on the timescale of its ring-down time τ . There may be no net decrease in the oscillator's amplitude during driving on an individual shot "to zero" *per se*. The applied rf during the driving interval merely brings the state of the oscillator (its amplitude and phase) into correlation with the magnetization at a given time, with such time determined by the weighting of the oscillator's measured trajectory. By properly weighting the resulting transient, an estimate of the state of the magnetization at a preferred time is obtained. It is *this weighting* that is meant to be suggested by the trajectories in both the before and after detection periods, and not a decay to zero amplitude of the oscillator. The possible effective length of the weighting function will be on the order of a few times T_{1a} .

A better way to view the detection period is that the applied inversion sequence brings the spin system into contact with the oscillator by providing a common spectral density at the oscillator frequency. Another interesting feature of the second-order method is that there is no need to restore an equilibrium magnetization. The *SNR* is independent of polarization, so the experiment's repetition rate is not limited by waiting for spin order. We have called this method of encoding spectra into the second-order signal Correlated Observations Narrow Quantum Uncertainty, Enhancing Spectroscopic Transients (CONQUEST)⁶⁻⁸.

5.3 BOOMERANG for Surface-Bound Samples

In Chapter 2 and in Appendix B, the expression for the force on a detector dipole (Equation (2.1)) exerted by a unit dipole of sample magnetization was used to find the sensor magnet shape that optimized the force signal-to-noise ratio for a sample contained in a spherical volume, and it was found that a right circular cylinder was nearly ideal and in fact the best shape given requirements of ease of manufacture and homogeneity. Consider now a circular “2-D” sample with given radius r_s , which could be composed of sites at an interface or a molecular monolayer deposited on a crystal surface. We can use Equation (2.1) to construct a force map in the vicinity of this flat sample to guide our design of a suitable sensor for this

sample’s magnetization. Figure 5.3 shows the force map. The picture suggests we use a circular cylinder with its radius approximately that of the sample.

Substitution of differential dipole elements into Equation (2.1) and integration over both a flat sample of radius r_s and surface magnetization density \overline{M}_s and a cylindrical detector magnet of radius a , height h , magnetization M_d , and distance from the sample R_{\max} yields the force

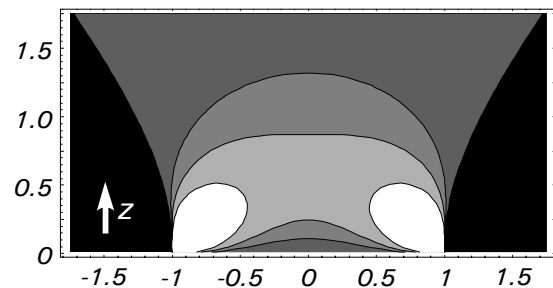


Figure 5.3. Force map over a flat circular sample. The sample is in the transverse plane perpendicular to the z -axis at $z=0$, and both the sample and the detector moments are aligned along the z -axis. Each contour represents a factor of two increase in the magnitude of the vertical force on a detector dipole at that location. The force is directed oppositely in the region colored black. Numerical labels on the axes represent distance in units of the sample's radius.

$$F_z = -\mu_0 \bar{M}_s M_d \sqrt{ar_s} \left(\frac{(2-m^2)K(m^2) - 2E(m^2)}{m} - \frac{(2-k^2)K(k^2) - 2E(k^2)}{k} \right), \quad (5.21)$$

where

$$m^2 = \frac{4ar_s}{(R_{\max} + h)^2 + (a + r_s)^2} \quad \text{and} \quad k^2 = \frac{4ar_s}{R_{\max}^2 + (a + r_s)^2} \quad (5.22a,b)$$

and where K and E are the complete elliptic integrals of the first and second kinds. When combined with the relevant expression for the force noise expected for a detector magnet attached to a massless suspension, the resulting signal-to-(Brownian)-noise ratio diverges as the R_{\max} parameter goes to zero. This limit is unrealistic anyway, as space to accommodate NMR coil windings and to provide adequate field homogeneity is required, as is relaxation of the zero-inert-mass approximation. We thus optimize the detector magnet's dimensions for a specific case only.

Suppose the sample is a 100 μm diameter circle with a surface density of one ^{13}C spin per square nanometer, and suppose we set R_{\max} equal to 10 μm . This might be the case were we to investigate chemical shift tensors at 125 MHz in an oriented monolayer of organic molecules deposited on an optical fiber, perhaps to see how the monolayer is modified by a covalently bound fluorophore in the fabrication of an immunosensor. In this case the optimal radius and height of the detector magnet are found to be 50.0 μm and 22.4 μm as shown in Figure 5.4. In that case the single-shot SNR is predicted to be about unity given an oscillator with a one-second ring-down time and $T_{1a} = 1$ s. In order to increase sensitivity, we have assumed that the polarization has been enhanced to 1% using optically polarized

^3He or ^{129}Xe . Polarization of solvents and of dissolved and surface species with noble gases are the subject of much recent interest⁹⁻¹², and polarization enhancements of 1000 have been reported at low fields in favorable cases. Whether enhancements to a few percent polarization can be made generally on surfaces is not clear, but surface species are likely to be particularly amenable to large and rapid enhancement.

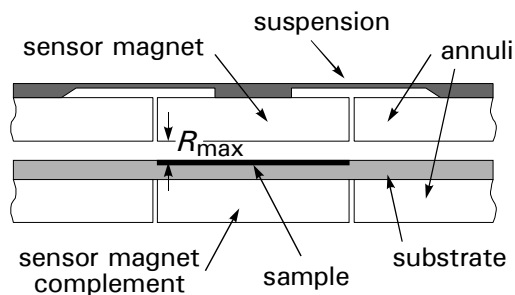


Figure 5.4. BOOMERANG for surface samples. The sensor magnet is drawn with dimensions that optimize sensitivity for the given sample radius and R_{max} .

The selection of a sample region in surface studies poses an interesting problem. One solution is to deposit the samples into the desired circular shape using a mask or ink-jet printer method. This would be convenient, especially for rapidly depositing many samples, but then the spectra might suffer from “edge effects” under some circumstances, where the chemical conditions at the edges of the sample disk are not indicative of the bulk of a more homogeneous surface. In that case it would be desirable to select a sample magnetically from a larger, more uniform film. Figure 5.5 shows how this might be accomplished with dc field pulses from a coil included in the apparatus for this purpose. The activated region could then be shuttled into a highly homogeneous field for evolution and then subsequently under a sensor magnet for detection.

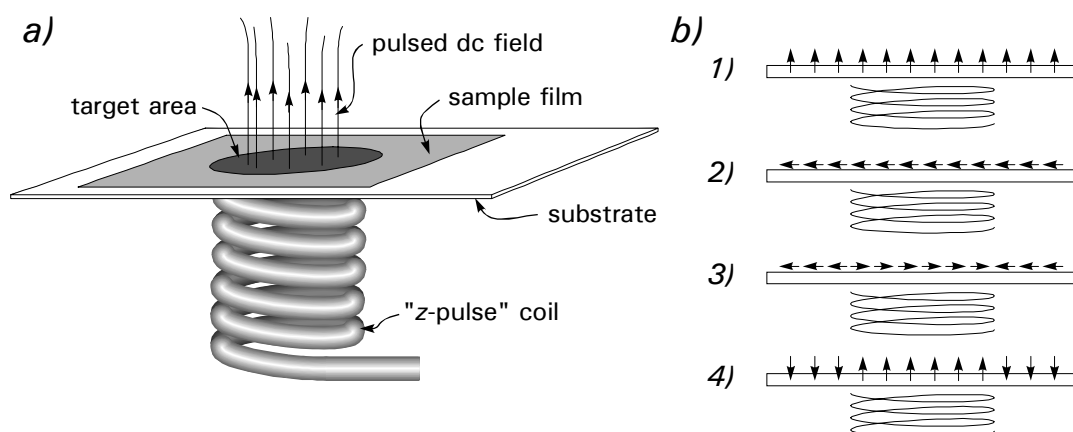


Figure 5.5. Magnetic selection of sample region. a) Substrate with sample film is slid into place over a coil that can produce a highly localized switched dc offset in the static field. b) Sample selection process. (1) Initial state. (2) $\pi/2$ pulse is applied to entire sample. (3) localized field ("z-pulse") is switched on long enough to advance the phase of the spins in the circular target area by π relative to surrounding spins. (4) $\pi/2$ pulse is applied to entire sample to create localized longitudinal magnetization for use in BOOMERANG.

5.4 Torsional BOOMERANG for Nanoscopic Samples

The analysis presented in Chapter 2 on scaling of the signal-to-noise ratio assumed that the frequency of the oscillator could be maintained in the audiofrequency range as the apparatus was scaled down for smaller samples. This can be done if the experimenter has independent control over the balance between elastic and magnetic spring constants or has other (active) means of control over the frequency³. However, this balance may become an increasingly difficult engineering challenge as the size scale of the detection apparatus is reduced into the sub-micron range. At higher frequencies, the increased rf power necessary to efficiently invert magnetization may cause other problems, such as heating of the sample or oscillator. It is therefore our concern in this section to address BOOMERANG with precessing or spin-locked *transverse* magnetization.

Figure 5.6 shows designs for BOOMERANG based on torsional resonance. The resonance frequencies of the moving parts coincide with the Larmor frequency of the spin system. The magnetic parts are all magnetized along the vertical in the figure as in longitudinal BOOMERANG, and this feature, perhaps in combination with external magnets not shown, provides a static field for the sample. However, the moving parts of the detector assembly are supported so as to make use of a net torque exerted by the sample's transverse magnetization.

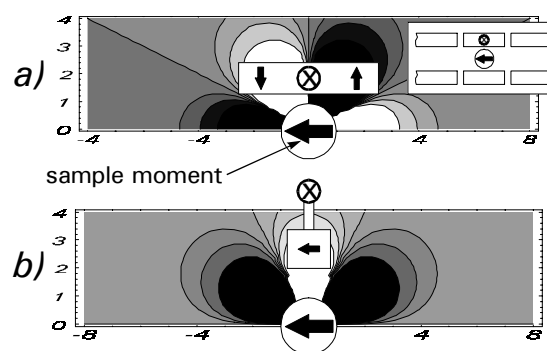


Figure 5.6. Force maps for design of torsional oscillators driven by transverse magnetization. Light and dark colors indicate forces of opposite sign. Each contour represents a factor of two increase in the magnitude of the force on a vertical detector dipole at that location. a) z-component of the force suggests a flat disk that undergoes torsional oscillations around the axis shown. b) x-component of the force suggests a pendulum-type oscillator. Numerical labels on the axes represent distance in units of the sample volume's radius. The inset to figure (a) shows the sensor as part of a BOOMERANG assembly.

It is known that torsional oscillators can have substantially better anchor losses¹³ than cantilevered or other longitudinal oscillators. The main reason is probably that the moving element's center of mass remains fixed, and so there is no momentum transfer to the substrate. This is also a feature of the sound-bars in mallet-percussion instruments like the xylophone, which are fixed to their supports at nodes in their fundamental mode of vibration. Figure 5.7 shows a sensor magnet fixed to an oscillator suspension based on this idea. Such xylophone designs might be useful at size scales where longitudinal detection is still practical but where eddy-current damping has been suppressed, and so anchor losses are predominant.

Unfortunately, magnetic materials are typically much more dense than silicon and other structural materials used in microfabrication. Calculations using magnetic masses fixed to a xylophone-bar oscillator show that there would have to be rather large inert ballast masses on both ends of the xylophone-bar in order to satisfy the desired condition that the magnetic mass lies entirely between the oscillator supports. This

inert mass lowers the detector's sensitivity for the case of a single sensor and a single sample. However, the figure suggests the possibility that these masses are not inert, but are instead other magnets driven by other samples.

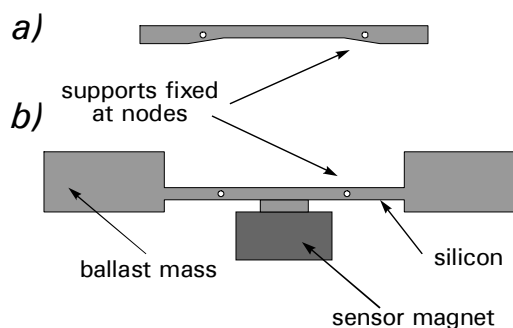


Figure 5.7. Xylophone-bar oscillators. a) Xylophone bar showing support points, which are nodes in the principal oscillatory mode by design. b) Silicon oscillator inspired by xylophone bar fixed to sensor magnet. Since magnet materials are so much more dense than silicon, substantial inert mass must be added to the oscillator. This suggests that more than one sensor oscillator be mechanically coupled together to drive a mode of a composite oscillator, with each sensor separately forced by its own sample.

5.5 Final Remarks – On Partitioning Samples and Microfabrication of Advanced Analytical Instruments

This chaining together of detector magnets each with its own sample is of far more than academic interest. One reason for such a composite detector is to improve sensitivity to average magnetization in a single sample that can be broken up into pieces. Suppose we have an NMR detection method whose SNR for a sample of linear dimension r is proportional to r^n . If the sample is broken into N

equal pieces, then the length scale of each piece is $r / N^{1/3}$ and the *SNR* from each piece will be proportional to $(r / N^{1/3})^n$ if its spectrum is measured with a detector optimized at the smaller size scale. An average of the signals from each piece should have a *SNR* $N^{1/2}$ times larger — $N^{1/2} (r / N^{1/3})^n = N^{1/2-n/3} \times r^n$.

This *SNR* expression exhibits a cutoff scaling factor, $n=3/2$, below which it should be possible to increase the signal-to-noise ratio simply by breaking up the sample. For example, in BOOMERANG on 3-D samples (where $n=1/2$), breaking up the sample results in a modest increase in sensitivity (proportional to $N^{1/3}$). As a flat sample's area scales only quadratically with r , *SNR* in BOOMERANG on 2-D samples is easily shown to have a scaling factor $n=-1/2$, and so surface BOOMERANG is particularly compatible with sensitivity enhancement by breaking up the sample (proportional to $N^{2/3}$). If it is possible to microfabricate massively parallel detectors at scales where instrument noise can be made negligible compared to spin noise, then a preferred approach for typical liquid samples would be to break each sample up as small as possible, as the *SNR* for second-order signals encoded with CONQUEST scales as r^0 (resulting in a sensitivity advantage to breaking up the sample that goes as $N^{1/2}$).[†] Designs, detailed microfabrication procedures, and preliminary results of microfabricated BOOMERANG devices are detailed by Madsen³.

[†] Conversely, for inductive detection ($n=2$), there is actually a very slight (proportional to $N^{1/6}$) advantage to *combining* samples (or merely putting them in the same NMR coil in different combinations).

The other reason for composite detectors brings up the much more general question of optimizing procedures and instrumentation to maximize extraction of information from a given *set* of samples. By combining microfabrication of detector arrays with micro-patterning of sample libraries, one could imagine building modes of a composite oscillator that are designed to be driven by *specific characteristics* of the whole library. Suppose, for example, that a surface is coated with an oriented enzyme-bearing lipid bilayer and a substrate is deposited so that its concentration is proportional to the function $\frac{1}{2} + \frac{1}{2}\cos kx$, where x denotes distance along some axis tangent to the surface. Then, if the concentration of a reaction product grows as the square of the substrate concentration (as in a second-order reaction, for example), there will be a component to the driving force on a composite oscillator during a suitably designed detection period at the spatial frequency $2k$, which will be absent if the reaction is first-order. Optimization procedures for such informational characteristics of sets of samples are an intriguing generalization of the theory of Chapter 2.

References

- 1 N. Wu, T. L. Peck, A. G. Webb, R. L. Magin, and J. V. Sweedler, *Anal. Chem.* **66**, 3849 (1994).
- 2 N. Wu, T. L. Peck, A. G. Webb, R. L. Magin, and J. V. Sweedler, *J. Am. Chem. Soc.* **116**, 7929 (1994).
- 3 L. A. Madsen, Ph. D. Thesis, California Institute of Technology, 2002.
- 4 T. George, *et al.*, in *IEEE Aerospace Conference* (Big Sky, Montana, 2001).
- 5 J. A. Sidles, J. L. Garbini, K. J. Bruland, D. Rugar, O. Züger, S. Hoen, and C. S. Yannoni, *Rev. Mod. Phys.* **67**, 249 (1995).
- 6 P. J. Carson, L. A. Madsen, G. M. Leskowitz, and D. P. Weitekamp, *Bull. Am. Phys. Soc.* **44**, 541 (1999).
- 7 P. J. Carson, L. A. Madsen, G. M. Leskowitz, and D. P. Weitekamp, U. S. Patent No. 6,081,119 (California Institute of Technology, USA, 2000).
- 8 P. J. Carson, L. A. Madsen, G. M. Leskowitz, and D. P. Weitekamp, U. S. Patent No. 6,087,872 (California Institute of Technology, USA, 2000).
- 9 S. Appelt, F. W. Haesing, S. Baer-Lang, N. J. Shah, and B. Blumich, *Chem. Phys. Lett* **348**, 263 (2001).
- 10 H. Desvaux, T. Gautier, G. Le Goff, M. Petro, and P. Berthault, *Euro. Phys. J. D* **12**, 289 (2000).
- 11 J. Smith, L. J. Smith, K. Knagge, E. MacNamara, and D. Raftery, *J. Am. Chem. Soc.* **123**, 2927 (2001).
- 12 T. Room, S. Appelt, R. Seydoux, E. L. Hahn, and A. Pines, *Phys. Rev. B* **55**, 11604 (1997).
- 13 T. A. Barrett, C. R. Miers, H. A. Sommer, K. Mochizuki, and J. T. Markert, *J. Appl. Phys.* **83**, 6235 (1998).